ACS APPLIED MATERIALS & INTERFACES

Research Article

www.acsami.org

Doping Magnesium Hydroxide with Sodium Nitrate: A New Approach to Tune the Dehydration Reactivity of Heat-Storage Materials

Alexandr Shkatulov,[†,‡] Tamara Krieger,[†] Vladimir Zaikovskii,[†,‡] Yurii Chesalov,[†,‡] and Yuri Aristov*[,†,‡]

[†]Boreskov Institute of Catalysis, Lavrentieva av., 5, Novosibirsk, Russia

[‡]Novosibirsk State University, Pirogova str., 2, Novosibirsk, Russia

Supporting Information

ABSTRACT: Thermochemical energy storage (TES) provides a challenging approach for improving the efficiency of various energy systems. Magnesium hydroxide, $Mg(OH)_2$, is known as a suitable material for TES at temperature $T > 300$ °C. In this work, the thermal decomposition of $Mg(OH)_2$ in the absence and presence of sodium nitrate ($NaNO_3$) is investigated to adapt this material for TES at $T < 300$ °C. The most notable observations described for the doped $Mg(OH)_2$ are (1) a significant reduction of the decomposition temperature T_d that allows tuning the dehydration reactivity by varying the $NaNO_3$ content. The T_d decrease by 25 °C is revealed at a salt content $Y \leq 2.0$ wt %. The maximum T_d depression of some 50 °C is observed at $Y = 15–20$ wt %; (2) the $NaNO_3$-doped $Mg(OH)_2$ decomposes considerably faster under conditions typical for closed TES cycles (at $T > 300$ °C in vapor atmosphere) than a pure $Mg(OH)_2$; (3) the morphology of the dehydration product (MgO) dramatically changes. Differential scanning calorimetry, high-resolution transmission electron microscopy, X-ray diffraction, X-ray photoelectron spectroscopy, and vibrational spectroscopy (IR and Raman) are used to study the observed effects and to elucidate possible ways the $NaNO_3$ influences the $Mg(OH)_2$ dehydration and morphology of the dehydration product. The mechanism involving a chemical interaction between the salt and the hydroxide accompanied by nitrate embedding into brucite layers is discussed.

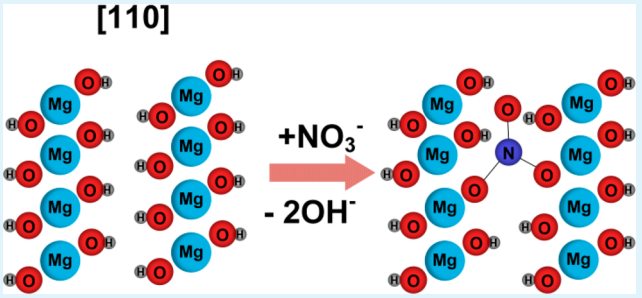

KEYWORDS: *magnesium hydroxide, brucite, dehydration kinetics, thermochemical heat storage, middle-temperature heat*

INTRODUCTION

Global problems of renewable energy and energy-saving technologies urge researchers to find new ways to transform and store energy. Development of novel efficient materials for generation and storage of electricity (fuel cells,[1] Li-batteries,[2,3] photovoltaics[4,5]), hydrogen,[6,7] and heat[8−10] can significantly advance the utilization of renewable energy and waste heat.

Heat storage can considerably improve the efficiency of energy units by ensuring a temporal coherence between heat production and heat consumption. Incorporation of a proper heat storage system reduces the amount of excess heat that would normally be wasted (Figure 1).[11]

Materials able to store large amounts of heat by reversible chemical reaction have attracted much attention in recent decades due to their higher heat storage capacities and the absence of thermal losses when compared to traditional sensible or latent heat storage materials.[8,9,11] Search for new materials for thermochemical energy storage (TES) with tunable properties that can be harmonized with a particular surplus heat source is an important goal in the area of energy-efficient and green technologies.

TES is based on a reversible chemical reaction[8]

$$AB \leftrightarrow A + B \quad (1)$$

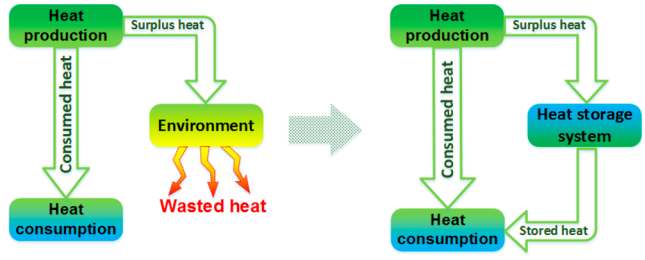

Figure 1. A schematic representation of heat-storage concept.

that allows absorption of heat in the course of an endothermic decomposition process. The reverse synthesis reaction is exothermic, which results in giving the stored heat back. The transition temperature T^* can be estimated under the stipulation that the change in the Gibbs free energy $\Delta G(T^*) = \Delta H(T^*) - T^*\Delta S(T^*)$ in the course of the reaction equals zero, $\Delta G(T^*) = 0$

Received: August 15, 2014
Accepted: October 21, 2014
Published: October 21, 2014

 © 2014 American Chemical Society

$$T^* = \Delta H(T^*)/\Delta S(T^*) \quad (2)$$

At $T > T^*$ decomposition and storage dominate, while at $T < T^*$ the synthesis reaction occurs, and heat is released. Hence, heat with the temperature potential T_h can be stored only if $T_h \geq T^*$ for the reaction used.

If substances AB and A are solids and B is a gas (vapor), according to the Gibbs phase rule, the system has one degree of freedom (monovariant system). Hence there is a one-to-one correspondence between the equilibrium gas pressure $P(B)$ and temperature T. It is given by the integral Van't Hoff equation $\ln P(B) = \exp(-\Delta G^\circ/RT)$ or

$$\ln P(B) = -\Delta H^\circ(T)/RT + \Delta S^\circ(T)/R \quad (3)$$

where ΔG°, ΔH°, and ΔS° stand for the variations of the standard Gibbs potential, enthalpy, and entropy in the course of reaction 1.

Alkali-earth metal hydroxides represent a class of thermochemical materials promising for TES at middle and high temperatures. Herein we consider the magnesium hydroxide decomposition (dehydration)

$$Mg(OH)_{2(sol)} = MgO_{(sol)} + H_2O_{(gas)} \quad (4)$$

To the best of our knowledge, this reaction was first suggested for long-term thermochemical storage of heat by Ervin.[12] This hydroxide has a high heat storage density (up to 1400 MJ/kg), is easily available, and is nontoxic.[8,13] The variations of the enthalpy and entropy in the course of reaction 4 are displayed in Table 1.

Table 1. Density ρ, Standard Enthalpy ΔH°_{298} and Enthalpy ΔS°_{298} of Formation[14]

	ρ, g/cm^3	ΔH°298, kJ/mol	ΔS°298, J/(mol·K)
$Mg(OH)_{2(sol)}$	2.36	−924.664	63.22
$MgO_{(sol)}$	3.58	−601.241	26.924
reaction 4		81.613	152.42

The equilibrium decomposition temperature can be estimated as $T^* = \Delta H^\circ(T^*)/\Delta S^\circ(T^*) = 536$ K = 263 °C at $P = 1$ bar. However, pure $Mg(OH)_2$ can not be effectively decomposed at this temperature, or even at $T < 300$ °C, because of its low dehydration rate. The temperature difference $(T - T^*) \approx 30-50$ °C serves as a driving force to initiate reaction 4. Therefore, in spite of its excellent thermodynamic characteristics, the unfavorable kinetics of pure $Mg(OH)_2$ decomposition prevents its widespread application. Indeed, more valuable heat with higher temperature potential must be used, which restricts the list of possible heat sources. Thus, the improvement of the decomposition reactivity at $T < 300$ °C is highly desirable. Several ways to reach this goal are considered in the literature.[15−19]

A promising approach to varying the dehydration temperature is the use of mixed hydroxides containing magnesium $Mg_xM_{(1-x)}(OH)_2$, where M = Ni and Co.[15,16] These materials are solid solutions with the brucite structure in which M^{2+} cations are incorporated instead of Mg^{2+}. They were prepared by coprecipitation from an aqueous solution. The mixed hydroxides lose water at a lower temperature than $Mg(OH)_2$, probably due to distortion of the brucite structure in the presence of nonmagnesium cations.

Another approach to promote the $Mg(OH)_2$ dehydration is a modification with an inorganic salt. Ishitobi et al. added lithium chloride to $Mg(OH)_2$ powder.[17] The authors claimed that the LiCl additive accelerates the $Mg(OH)_2$ dehydration at $T < 300$ °C. Similar effects have recently been reported for lithium bromide;[18] however, no detailed study of the observed effect was performed. The authors assumed that the acceleration arises from the hydrophilic properties of the salts that absorb water vapor thus reducing its partial pressure near the $Mg(OH)_2$ surface.

Despite the above-mentioned efforts there is still much room for new modifying techniques, synthesis, and study of new materials for TES at $T < 300$ °C. The present article addresses the effect of sodium nitrate on the dehydration of magnesium hydroxide to adapt this material for TES at $T < 300$ °C. The authors selected this salt because it was assumed, in ref 19, that modification with $NaNO_3$ may produce significant reduction of the dehydration temperature of $Mg(OH)_2$ deposited into the pores of expanded vermiculite.

Here we will make emphases on thermal behavior of $NaNO_3$-doped $Mg(OH)_2$ and characterization of the dehydration products. In the majority of the reviewed papers $Mg(OH)_2$ dehydration was studied under vacuum. In this research we study the dehydration kinetics at a fixed pressure of pure water vapor that is typical for TES with closed cycles.[8] Differential scanning calorimetry (DSC), High-resolution transmission electron microscopy (HR-TEM), X-ray diffraction (XRD), X-ray photoelectron spectroscopy (XPS), and Brunauer−Emmett−Teller (BET) analysis were used to study the effects observed and analyze the influence of $NaNO_3$ on the $Mg(OH)_2$ dehydration.

EXPERIMENTAL SECTION

Materials Preparation. Reference magnesium hydroxide and magnesium oxide (hereinafter referred to as MH and MO, respectively) were prepared as follows. Commercially available MgO (Reahim, >99.0%) powder was preliminarily calcined at 800 °C to remove carbonate and hydroxide impurities and then mixed with degassed distilled water. The mixture was sealed in an autoclave and kept at $T = 110$ °C for 24 h. These conditions are comparable with the conditions of three-phase hydration, described in ref 20, which ensure high hydration conversions after several hours. Excessive amount of time is required for the material to undergo aging. The product was filtered, abundantly washed by distilled degassed water, and dried at $T = 120$ °C for 12 h. The reference magnesium oxide MgO was prepared by calcination of MH at 350 °C for 4 h. Both MO and MH were stored hermetically in a vacuum desiccator.

A series of samples ($Mg(OH)_2$ + $NaNO_3$) were then prepared with various salt content. MH and $NaNO_3$ powder (>99.8%) were mixed to the desired composition (Table 2). To gain a uniform distribution of the salt, the mixing was followed by addition of water and subsequently evaporated at 60 °C in a vacuum under vigorous stirring on a rotary evaporator. For ease of notation, the obtained samples of (sodium nitrate)/(magnesium hydroxide) will be referred to as SN/MH-Y, where Y represents the salt content in weight % (Table 2).

The SN/MH-Y were calcined in air at 350 °C for 4 h to obtain dehydrated samples designated as SN/MO-Y. SN/MO-Y with $Y = 0.5$,

Table 2. Content $NaNO_3$ in SN/MH-Y

sample	Y ($NaNO_3$), wt %
SN/MH-0.5	0.49
SN/MH-2	2.02
SN/MH-5	5.01
SN/MH-10	10.0
SN/MH-15	15.0
SN/MH-20	20.0

2, 5, and 10% were rehydrated by saturated water vapor at T = 80 °C (samples SN/MO-Y-r).

Material Characterization. The dehydration was studied by DSC and thermogravimetric analysis (TGA) in a controlled atmosphere. To provide a deeper insight into the effect of $NaNO_3$ on the $Mg(OH)_2$ dehydration we studied the phase composition by XRD analysis and the texture by HR-TEM and BET techniques.

Differential Scanning Calorimetry. The DSC measurements were carried out with a NETSCHZ DSC 404C apparatus at a constant heating rate (15 K/min) in dry argon flow (200 mL/min). Prior to measurement a specimen (~10 mg) was put in an open standard 25 μL aluminum crucible. As a reference we used an empty crucible. The K-type thermocouple was calibrated (temperature and sensitivity) under the same conditions with a standard (DIN 51 007) calibration set (In, Bi, Sn, Zn, CsCl).

The dehydration temperature was characterized by either onset temperature T_{onset} or peak temperature T_{peak}. The former temperature is commonly ascribed to the beginning of dehydration, while the latter is ascribed to the maximum dehydration rate.

The dehydration heat Q (J/g) was estimated as

$$Q = \frac{1}{\beta}\int_{T1}^{T2} E(T)\cdot I(T)\mathrm{d}T \tag{5}$$

where β (K/s) is the heating rate, T_1 and T_2 are the extreme temperatures, I (μV/mg) is a thermocouple signal, and E (mW/μV) is a sensitivity function established by preliminary calibration.

The DSC curves were measured in the range T = 30−450 °C. For each material the DSC parameters (T_{onset}, T_{peak}, and Q) were averaged over four tests. A confidence interval of the random error was calculated with Student's t-distribution corresponding to the probability of 0.975.

Powder X-ray Diffraction. The XRD analysis was performed using a Siemens D-500 diffractometer equipped with a heater. The XRD patterns were recorded with Cu Kα radiation filtered by a graphite monochromator. The experiments were conducted in air in the range T = 150−350 °C. The scanning was carried out in 2θ intervals of 10−70° at room temperature and of 27−45° at elevated temperatures. The step of scanning was 0.05°, while the accumulation time was 1 s.

The size D of coherent scattering region was estimated with the Scherrer equation[21]

$$D = \frac{K\cdot\lambda}{\Delta_{1/2}\cdot\cos\theta} \tag{7}$$

where K is the Scherrer constant (K = 0.9 for spherical particles), $\Delta_{1/2}$ is the peak width on half-height, and θ is the reflection angle.

N_2 Adsorption Isotherms. The porous structure of the samples was examined by N_2 adsorption at 77 K with a NOVA 1200e Pore Analyzer at P/P_0 = 0.005−0.995. Before measurement, the sample (~100 mg) was degassed in vacuum at 150 °C for 180 min. The surface area was calculated by the BET method with the area of N_2 molecule taken as 0.162 nm^2 and P/P_0 = 0.05−0.35.

High-Resolution Transmission Electron Microscopy. As $Mg(OH)_2$ is very sensitive to electron beam heating, this study is limited to low magnification, where dehydroxylation rates could be somehow restricted.

HR-TEM images were obtained on a JEM-2010 electron microscope (JEOL, Japan) with a lattice-fringe resolution of 0.14 nm and at an accelerating voltage of 200 kV. Samples to be examined by HR-TEM were prepared on a perforated carbon film mounted on a copper grid. The high-resolution images of periodic structures were analyzed by the Fourier method. The kinetics of $Mg(OH)_2$ dehydration are commonly studied either under vacuum or inert atmosphere.[22−25] In this study the kinetics were examined at a fixed water vapor pressure of 22.2 mbar over the sample. This is the saturated vapor pressure at 19 °C, which corresponds to typical conditions during the dehydration stage of a TES unit with a closed operation cycle: a reactor filled with $Mg(OH)_2$ is commonly linked with a condenser where liberated water is collected.[8]

Thermogravimetry. The dehydration kinetics were measured by a TGA technique under isothermal conditions. The weight loss curves were recorded using a Rubotherm TGA unit with a magnetic suspension balance. After loading into the reaction chamber, the samples (~50 mg) were dried at 120 °C in vacuum to remove adsorbed water. Then, water vapor was introduced into the measuring cell by connecting it to a condenser maintained at 19 °C. The temperature was quickly raised to the desired one, and the weight loss curve was recorded.

The dehydration kinetics were measured at 260, 270, 280, 290, and 300 °C. After the measurements, dry sample mass m_d was determined by evacuating the measuring cell and heating it to 350 °C. The error of the weight measurement is estimated to be $\pm 10^{-5}$ g.

The dehydration fraction α is determined as

$$\alpha = \frac{m_0 - m(t)}{m_0 - m_d} \tag{8}$$

where m_0 is the initial sample mass, and $m(t)$ is the current sample mass.

Vibrational Spectroscopy (IR and Raman). Attenuated total reflectance−Fourier transform infrared (ATR-FTIR) spectra (4000−250 cm^{-1}, 32 scans, resolution 4 cm^{-1}) were obtained using an Agilent Technologies Cary 660 FTIR spectrometer and a PIKE Technologies GladiATR accessory with a diamond crystal.

Fourier transform Raman (FT-Raman) spectra (3600−150 cm^{-1}, 300 scans, resolution 4 cm^{-1}, 180° geometry) were recorded using a Bruker RFS 100/S spectrometer. Excitation of the 1064 nm line was provided by a Nd:YAG laser (100 mW power output).

X-ray Photoelectron Spectroscopy. XRP experiments were performed with an ES-300 Kratos analytical photoelectron spectrometer with Al anode. Samples were fixed in the analyzer chamber on double-faced vacuum adhesive tape. The spectra were recorded using an X-ray source at power of 200 W (~14 kV, 14 mA).

The spectrometer was calibrated using bulk gold (Au $4f_{7/2}$) and copper (Cu $2p_{3/2}$) photoelectron peaks with the binding energy values of 84.0 and 932.7 eV, respectively. The position of the Mg 2p peak (49.5 eV) was used as a standard reference for calibration of Mg-containing samples. The chemical composition of the surface was determined from the integral peak areas using standard atomic sensitivity factors (ASF).[26] The curve-fitting procedure was performed using an approximation based on a combination of the Gaussian and Lorentzian functions with subtraction of a Shirley-type background. Before curve fitting, all experimental spectra were smoothed using a Fourier filter. Processing of the obtained data and spectral analyses were performed using PS-Calc program.

RESULTS

Differential Scanning Calorimetry. The DSC technique was used to quantify both the temperature and the heat of $Mg(OH)_2$ dehydration. The DSC curves of doped hydroxides (SN/MH-Y) exhibit an intensive endothermic peak that arises from the $Mg(OH)_2$ dehydration. The position of the peak depends on the $NaNO_3$ content: the peak temperature decreases from 411.0 ± 0.7 °C to 367.6 ± 1.2 °C when the $NaNO_3$ content increases from 0 to 20 wt % (Figure 2). It can be seen that even small quantities of $NaNO_3$ ($Y \leq 2$ wt %) considerably affect the dehydration; for example, an 0.5% $NaNO_3$ additive reduces both T_{onset} and T_{peak} by ~25 °C. The maximum decrease of decomposition temperature (~50 °C) is observed at $Y \geq$ (15−20) wt %. Thus, varying the $NaNO_3$ content is an efficient and convenient tool for managing the $Mg(OH)_2$ dehydration temperature within ~50 °C range below that of pure MH.

The dehydration heat normalized per 1 g of SN/MH-Y decreases from 1325 to 1040 J/g almost linearly with the increase in salt content (Figure 3).

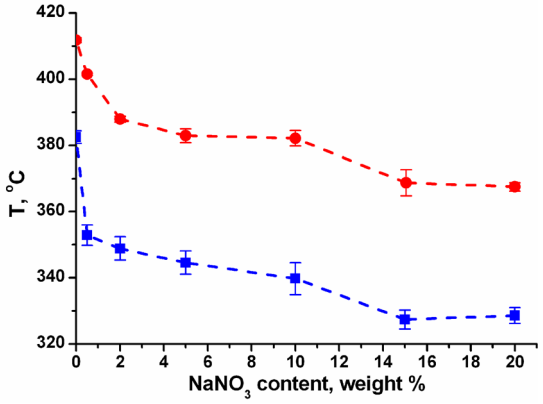

Figure 2. Dehydration temperatures T_{onset} (■) and T_{peak} (●) for SN/MH-Y.

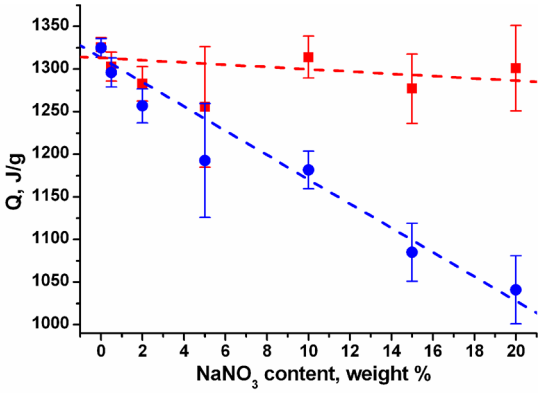

Figure 3. DSC dehydration peak areas for SN/MH-Y: (●) J/(g of the mixture), (■) J/(g of $Mg(OH)_2$).

This reduction mainly originates from the decrease in the hydroxide fraction in SM/MH-Y. Indeed, the heat renormalized per 1 g of $Mg(OH)_2$ remains nearly constant (1285 J/g) at Y = 2−20% within a random error of 3% and is only slightly lower than for the reference MH. Hence, at $Y \leq 10\%$ a significant reduction of the dehydration temperature is accompanied by only small decrease in the dehydration enthalpy, which still allows a high heat storage capacity of (1240 ± 50) J/(g of material).

At large salt contents ($Y \geq 10\%$), a subtle endothermic effect appears at 308 °C (Figure S1 and Table S1 in the Supporting Information). This effect can be ascribed to a melting of crystalline $NaNO_3$.[27] The apparent specific heat of $NaNO_3$ melting obtained by the peak integration at Y = 20% is ∼5 J/g. This value is lower than that calculated from pure $NaNO_3$ melting heat[28] and $NaNO_3$ content in SN/MH-Y (38 J/g). Therefore, the state of sodium nitrate in the mixtures SN/MH-Y is very different from that in bulk. This may result from interaction between the salt and hydroxide. A second-order phase transition (λ-transition) that is observed in bulk crystalline $NaNO_3$ at 276 °C can be tentatively detected only at Y = 20%, which is probably due to its very low heat effect.[29]

Isothermal Dehydration Kinetics. The kinetic curves of MH dehydration under water vapor atmosphere exhibit a pronounced induction period (Figure 4). This sigmoid behavior is typical for nucleation and growth kinetic models, and differs from dehydration under vacuum or inert gas conditions that commonly exhibit exponential dynamics.[22−25]

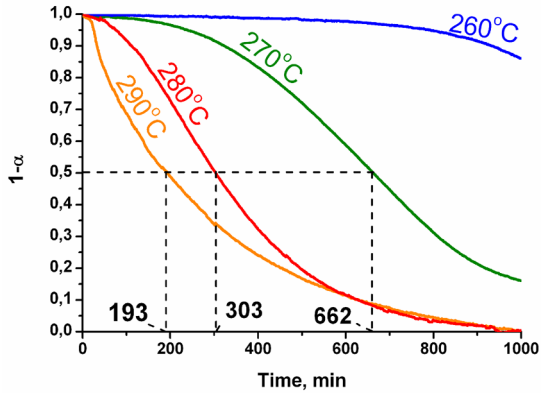

Figure 4. Dehydration kinetic curves for MH at $P(H_2O)$ = 22.2 mbar. The half-conversion times are given on the graph.

The higher the temperature, the more rapidly the dehydration proceeds: the induction period dramatically decreases at higher temperature and almost disappears at 290 °C (Figure 4). The induction period may be associated with the kinetic manifestation of surface nuclei formation slowed due to the presence of water at the $Mg(OH)_2$ surface. On the contrary, under the same conditions, the dehydration of SN/MH-10 occurs without any induction period and can be described by an exponential equation (Figure 5). This "sigmoid to exponential"

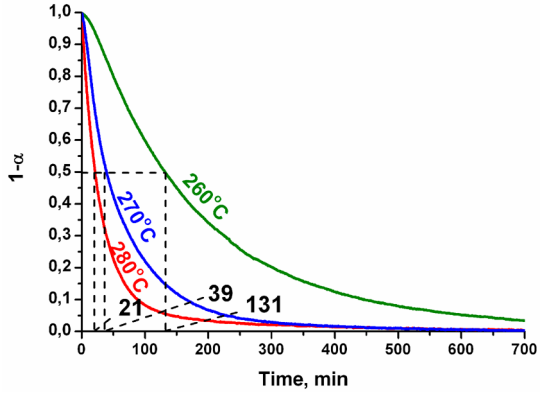

Figure 5. Dehydration kinetic curves for SN/MH-10 at $P(H_2O)$ = 22.2 mbar. The half-conversion times are given on the graph.

transformation of the dehydration dynamics caused by the $NaNO_3$ addition may indicate drastic changes in the dehydration pathways as discussed later.

The times of half-conversion, $\tau_{0.5}$, for SN/MH-10 dehydration measured at T = 260−280 °C and $P(H_2O)$ = 22.2 mbar are less than those for MH by a factor of 10−15 at the same conditions (Figure 4 and 5). The value of $\tau_{0.5}$ at 290 °C could not be measured because the decomposition proceeds before the sample has reached this temperature ($\tau_{0.5}$ < 10 min). Hence, the $NaNO_3$ additive considerably facilitates the dehydration of $Mg(OH)_2$ at T < 300 °C and the pressure typical for closed TES cycles (20−30 mbar). Plots of the $\ln(\tau_{0.5})$ versus $1/T$ are straight lines (Figure S2 and Table S2 in the Supporting Information) for both MH and SN/MH-10 with the slopes formally corresponding to the activation energy of (164 ± 10) and (224 ± 40) kJ/mol, respectively. Both activation energies are higher than 80−125 kJ/mol reported for the $Mg(OH)_2$ dehydration in vacuum or inert atmosphere.[17,30,31] This may be related to hindered water removal

dx.doi.org/10.1021/am505418z | ACS Appl. Mater. Interfaces 2014, 6, 19966−19977

during dehydration due to the presence of water vapor over the sample. The salt is likely to additionally bind the releasing water. The activation entropy drops from −(249 ± 16) J/(mol·K) for MH to −(382 ± 66) J/(mol·K) for SN/MH-10. This suggests that the structural factors could be more important in activating the $Mg(OH)_2$ dehydration by the salt than the energetic factors.

Powder XRD Analysis. The room-temperature X-ray powder diffraction pattern of MH (Figure 6) exhibits only a

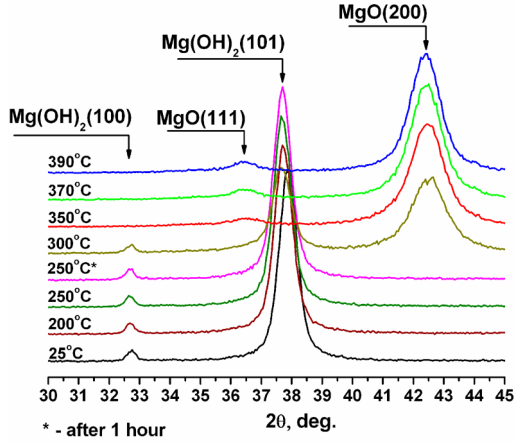

Figure 6. XRD patterns for MH at various temperatures.

hexagonal brucite phase (PDF No. 84−2163) with the lattice parameters (a = 3.148(6) Å, c = 4.771(3) Å).[32] At 300 °C, MH partially dehydrates yielding a cubic phase of periclase (MgO, PDF No. 89−7746) according to reaction 4.

The transformation manifests itself in the emergence of MgO (200) peak with simultaneous depression of $Mg(OH)_2$ (100), (101), and (111) reflexes. The brucite−periclase transformation in MH starts between 250 and 300 °C. At $T \geq$ 350 °C, only the periclase phase is detected. XRD peaks of brucite detected in SN/MH-10 are identical to those in MH. In both materials, brucite exhibits a well-defined lamellar structure since the sizes of the coherent scattering region (CSR) $D_{001,011}$ are 5−15 nm (SN/MH-10) and 12−16 nm (MH), while D_{110} is 40 nm for both samples.

The first traces of the brucite-to-periclase transformation in SN/MH-10 appear at 220−230 °C, and the process is complete at 260 °C (Figure 7). Thus, the transformation temperature

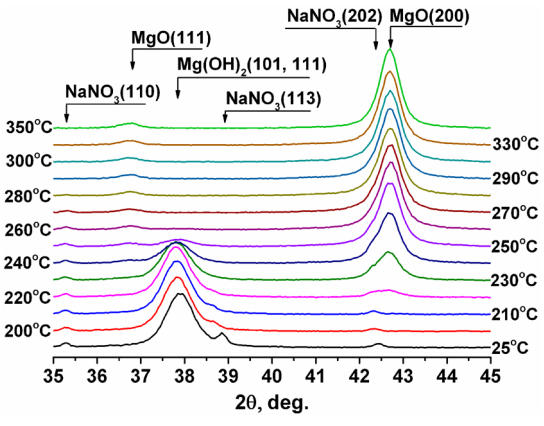

Figure 7. XRD patterns for SN/MH-10 at 2θ = 35−45°.

reduces by some 50 °C as compared with that for MH. The value of the temperature depression agrees well with the DSC data (Figure 2) despite the dehydration in the DSC cell being recorded at a much higher temperature due to the dynamic character of the DSC measurements and relatively high heating rate (15 K/min).

XRD peaks of $NaNO_3$ detected for SN/MH-10 at 25 °C show that the salt forms an α-phase (PDF No. 89−0310). As the temperature increases, all the $NaNO_3$ peaks shift to smaller angles due to a thermal drift (Figure 8).

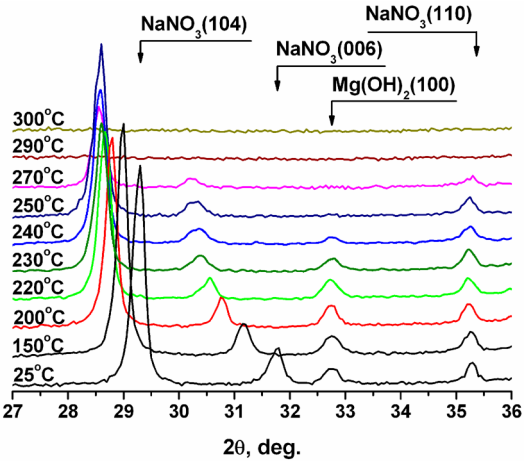

Figure 8. XRD patterns for SN/MH-10 at 2θ = 27−36°.

Broadening of the $NaNO_3$ peaks at 220−270 °C (Figures 7 and 8) may be due to disordering of $NaNO_3$ phase caused by its interaction with $Mg(OH)_2$ and/or MgO. The salt reflexes vanish in the narrow temperature range between 270 and 290 °C due to a threshold process that is different than salt melting alone (the latter takes place at 308 °C[27]). After it cools to 25 °C, $NaNO_3$ crystallizes again in α-phase.

The observed salt transformation at 270−290 °C (Figure 8) can not be a reason for the brucite-to-periclase transformation in SN/MH-10 at 230−250 °C (Figure 7). On the contrary, the broadening of the $NaNO_3$ peaks starts right at 220 °C and thus may be caused by the salt interaction with the initial brucite phase occurring at this temperature.

The size of CSR of the resulting MgO is 6−8 nm (Table 3), which is consistent with literature data.[22,33,34] The MgO surface

Table 3. Size (in nm) of Coherent Scattering Regions for MgO Crystals

MH		SN/MH-10	
T, °C	MgO (200)	T, °C	MgO (200)
300	6.5	250	29.0
350	6.5	250 (1 h)	33.0
370	7.5	300	32.5
390	7.5	25	33.0

area S, estimated assuming MgO crystallites to be cubes, is 300−340 m^2/g. The MgO crystallites in SN/MO-10 are ∼4 times larger (the CSR size is 30−33 nm), which corresponds to S = 70−80 m^2/g.

BET Analysis. The surface area of the initial MH was measured as 14 m^2/g, which is close to values reported in the literature.[35] This area corresponds to a particle size of 180 nm,

dx.doi.org/10.1021/am505418z | ACS Appl. Mater. Interfaces 2014, 6, 19966−19977

which is in rough agreement with the size (130 nm) estimated from the width of (101) reflex; the difference may be related to the particle geometry. Enlargement of the MgO particles and lowering the MgO specific surface area is confirmed by BET analysis: the surface area for SN/MO-Y gradually decreases from 265 m^2/g (Y = 0% (MH)) to 20 m^2/g (Y = 20%) (Figure 9). The BET areas are lower than those estimated from the CSR size. This may be because some of the MgO intergrain surface area, which contributed to scattering, is not available for N_2 adsorption.

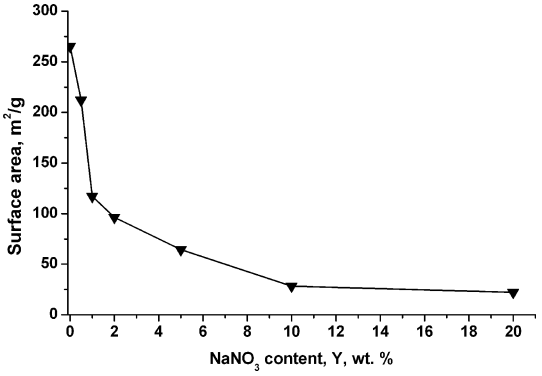

Figure 9. Specific surface area of SN/MO-Y at various salt content.

Electron Microscopy. $Mg(OH)_2$ has a hexagonal lattice and forms the hexagonal platelets of 200−250 nm size that can be seen for MH in TEM micrographs (Figure 10). The doping by $NaNO_3$ does not change either the size or the morphology of the $Mg(OH)_2$ particles (Figure S3 in the Supporting Information). The MgO particle obtained by MH dehydration at 350 °C retains the overall shape and size of the initial $Mg(OH)_2$ crystals; that is, a pseudomorphism is observed. Figure 10a shows that the pseudomorph consists of hexagonal 200−500 nm agglomerates formed by intergrown 2−3 nm MgO particles. The agglomerates have a well-distinguished slit-shaped structure (Figure 10b). This observation is consistent with the (rapid nucleation)/(slow growth) model of $Mg(OH)_2$ dehydroxilation proposed by McKelvy[36,37] and other data reported in the literature.[38,39]

The morphology of MgO particles in SN/MH-10 calcined at 350 °C dramatically differs from that in the reference MH. SN/MO-10 consists of irregular MgO crystallites (Figure 10c); hence, the pseudomorph is destroyed in the presence of $NaNO_3$. The crystallites are intergrown and have the sizes of ∼20−30 nm, which is in accordance with the X-ray data. Under the mild conditions of dehydroxylation (T = 260 °C, $P(H_2O)$ = 22.2 mbar, ∼48 h) an intermediate state is observed in which coarser and better-crystallized particles of MgO are formed (Figure S4 in the Supporting Information).

The $NaNO_3$ cannot be observed on the micrographs because it was eliminated during preparation of the sample for the HR-TEM. This was done to avoid any sudden decomposition of the salt by the electron beam/high temperature.

Raman and FTIR Spectra. The Raman spectra of the initial samples, namely, SN/MH-2 and SN/MH-10, measured over a range of 500 to 1500 cm^{-1} exhibit bands at 445 and 280 cm^{-1} due to lattice modes of brucite $Mg(OH)_2$.[40] The bands at 1386, 1068, 726, and 186 cm^{-1} assigned to vibrations of calcite-type $NaNO_3$[41,42] are also observed in these spectra (Figure 11a).

For the same samples after dehydration and subsequent rehydration, the most intense peak at 1068 cm^{-1} is split, and a broad peak at ∼1053 cm^{-1} appears (Figure 11b). This peak is dominant at Y = 2% and manifests itself as a shoulder at Y = 10%. It is assumed that during sample dehydration and/or subsequent rehydration a part of the salt interacts with

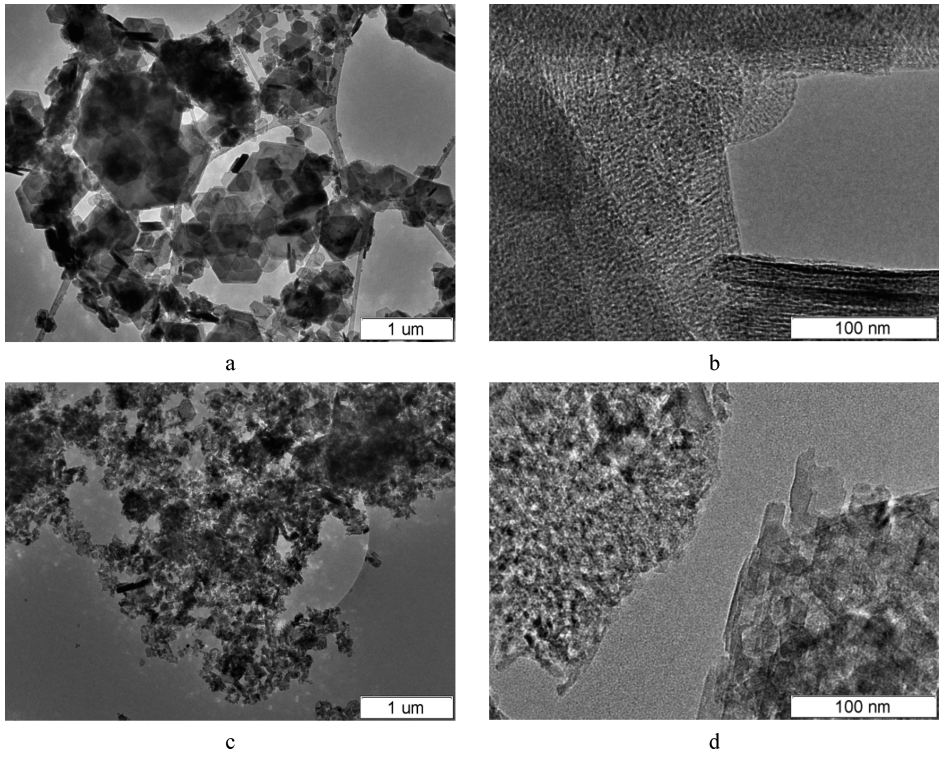

Figure 10. HR-TEM images of MO (a, b) and SN/MO-Y (c, d).

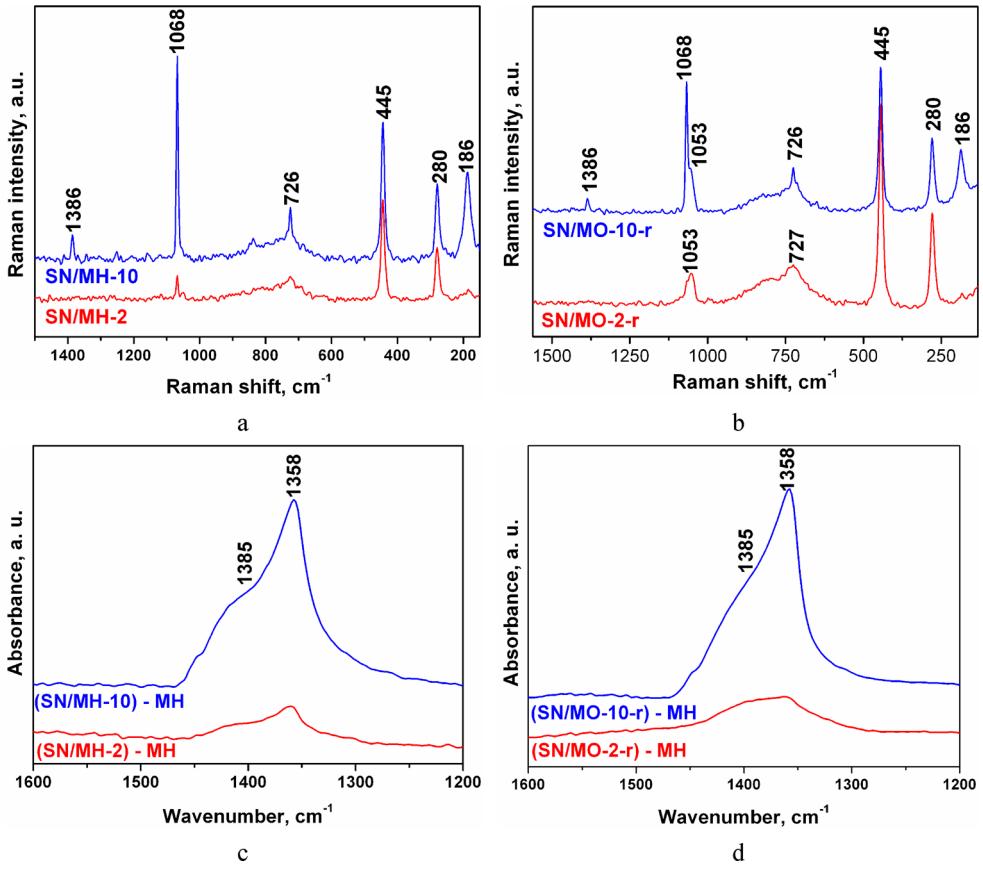

Figure 11. Differential Raman (a, b) and IR (c, d) spectra of initial SN/MH-Y (a, c) and rehydrated SN/MO-Y-r (b, d).

$Mg(OH)_2$ to form a highly defective and disordered phase in which the geometry of nitrate ion is somehow distorted. The distortion leads to appearance of the broad Raman peak located at 1053 cm^{-1}, traces of which can be discerned for SN/MH-2 and SN/MH-10 (Figure 11a), too. In addition, the distortion of the nitrate-ion geometry results not only in the disappearance of the band at 186 cm^{-1} due to the lattice vibrations of calcite-type $NaNO_3$[42] from the spectrum of the SN/MH-2 sample but also in a considerable broadening of band at 726 cm^{-1} assigned to the doubly degenerate E′ mode of nitrate-ion. The broadening of this band is probably associated with the reduction of nitrate-ion symmetry.

Similar splitting/broadening is found for SN/MH-2 and SN/MH-10 by FTIR technique. Broad absorption at 1300−1500 cm^{-1} is nonsymmetric and presumably consists of two bands (Figure 11c,d). A quite narrow band at 1405 cm^{-1} was detected in the spectrum of calcite-type $NaNO_3$ and is attributed to E_u vibration.[41] Its relative contribution increases at larger *Y*. The broad band at 1358 cm^{-1} appears at low salt contents, probably as a result of the salt-hydroxide interaction. A broadening of the band at 1385 cm^{-1} assigned to the doubly degenerate E′ mode of the nitrate ion is associated apparently with the reduction of nitrate-ion symmetry. Similar patterns are observed for dehydrated (not shown) and rehydrated samples; FTIR spectra of the initial and rehydrated samples are close (Figure 11c,d).

X-Ray Photoelectron Spectroscopy. To get insight into the mode of fixation of $NaNO_3$ and/or its interaction with the pure hydroxide, the material was studied by X-ray photoelectron spectroscopy. The binding energies of Mg 1s, Mg 2s, and O 1s remain unchanged for MH, SN/MH-10, and SN/MH-10 after dehydration and subsequent rehydration (not presented) and are close to the values observed for bulk $Mg(OH)_2$. However, the shape of O 1s peak slightly changes due to the increased contribution of the component with the binding energy of 531.4 eV responsible for the O−H bonds (Figure S5 in the Supporting Information).

Another important finding concerns the surface atomic ratio [N]/[Na] that appears to be constant for $NaNO_3$ and SN/MH-10 but approaches zero for the rehydrated sample, whereas the surface ratio [Mg]/[Na] does not change after rehydration (Table 4). This indicates that nitrogen atoms leave the surface of the samples, while Na conserves. Therefore, Na and N become uncoupled in the rehydrated sample.

Table 4. Atomic Ratios [N]/[Na] and [Mg]/[Na] for Various Samples

sample	[N]/[Na]	[Mg]/[Na]
$NaNO_3$	0.37	
SN/MH-10	0.37	0.16
SN/MH-10-r	~0	0.17

DISCUSSION

This study has revealed the following findings on the decomposition of $Mg(OH)_2$ through modification with sodium nitrate: (1) the temperature threshold for SN/MH-Y dehydration is notably lower than the temperature threshold for pure MH, which is indicative of an enhanced decomposition rate at $T < 300$ °C ; (2) $NaNO_3$ disordering is observed at the same temperature range when the decomposition starts; (3) the morphology and textural properties of the resulting MgO

dx.doi.org/10.1021/am505418z | ACS Appl. Mater. Interfaces 2014, 6, 19966−19977

dramatically change in the presence of $NaNO_3$; (4) the vibrational spectra suggest that part of the NO_3^- ions lower their symmetry; (5) the XPS study reveals uncoupling of N and Na atoms and the increase of O−H fraction on the surface of SN/MH-10-r. It is assumed that these findings stem from the $NaNO_3$ impact on the thermodynamics and/or kinetics of reaction 1, which intimately affects the decomposition pathways of $Mg(OH)_2$.

The Reaction Thermodynamics. Since both the initial reagent and final product are porous, the effect of $NaNO_3$ may be due to specific contributions of the surface energy and entropy. Indeed, the increase in the $NaNO_3$ content Y results in simultaneously lowering the specific surface area of the product, SM/MO-Y, and reducing the dehydration temperature of SM/MH-Y (Figure 2). The lower surface area is expected to result in smaller surface energy of the product. This is profitable from a thermodynamic point of view and may be a reason for the observed depression of the dehydration temperature.

Estimating the effect of surface energy on the dehydration temperature, the variation of the Gibbs free energy $\Delta_r G^o$ for reaction 4 consists of the bulk and surface (interfacial) terms;

$$\Delta_r G^o = \Delta_{bulk} G^o + \Delta_{surf} G^o \quad (9)$$

The bulk Gibbs energy can be written as

$$\Delta_{bulk} G^o = \Delta_f G^o_{pro} - \Delta_f G^o_{rea} = [\Delta_f G^o(MgO_{bulk}) + \Delta_f G^o(H_2O)] - \Delta_f G^o(Mg(OH)_{2bulk}) \quad (10)$$

where $\Delta_f G^o_{pro}$ and $\Delta_f G^o_{rea}$ are the formation free energies of the bulk products and reagents, respectively. The dependences $\Delta_f G^o_{pro}(T)$ and $\Delta_f G^o_{rea}(T)$ are calculated at $P(H_2O) = 1$ bar. The equilibrium dehydration temperature in bulk T^*(bulk) is determined by the condition $\Delta_{bulk} G^o = 0$ or $\Delta_f G^o_{pro} = \Delta_f G^o_{rea}$. It corresponds to the intersection of the lines $\Delta_f G^o_{pro}(T)$ and $\Delta_f G^o_{rea}(T)$ (point A on Figure 12) that gives T^*(bulk) = 536 K = 263 °C.

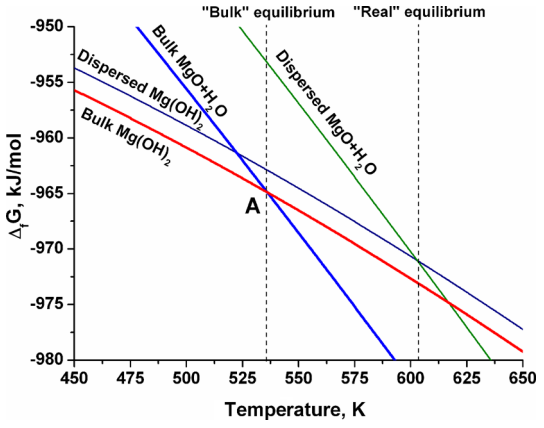

Figure 12. Schematic effect of the interfacial energy on the $Mg(OH)_2$ dehydration temperature.

Under real conditions of reaction 4, the solid phases are porous so that the surface free energies $\Delta_{surf} G^o_{pro}$ and $\Delta_{surf} G^o_{rea}$ must be taken into account. If they are equal, $\Delta_{surf} G^o = \Delta_{surf} G^o_{pro} - \Delta_{surf} G^o_{rea} = 0$, the dehydration temperature does not change. If $\Delta_{surf} G^o_{pro} < \Delta_{surf} G^o_{rea}$, the dehydration temperature will decrease with respect to that in bulk. It will accordingly increase if $\Delta_{surf} G^o_{pro} > \Delta_{surf} G^o_{rea}$. The latter case is likely to be realized for the reference MH (Y = 0%), because its specific surface area (S_{rea} = 13.8 m^2/g) is much smaller as compared with that of the product (S_{pro} = 265 m^2/g, Figure 9). That may lead to an increase in the dehydration temperature much above T^*(bulk) = 263 °C (Figure 12).

For increasing Y, the product (SM/MO-Y) becomes less disperse, which results in lowering the $\Delta_{surf} G^o_{pro}$ value and, hence, reduces the dehydration temperature with respect to the case of Y = 0. The surface energy $\Delta_{surf} G^o$(MgO) of MgO in SM/MO-Y (J/g) is estimated from the specific surface energy E_s of anhydrous MgO and the specific surface area S_{pro} of MH and SN/MH-Y (Figure 9)

$$\Delta_{surf} G^o(MgO) \approx E_s \cdot S_{pro} \quad (11)$$

The MgO surface energy was previously reported to be 1.0,[43] 1.1,[44] and 1.15[45] J/m^2. The surface energy $\Delta_{surf} G^o$(MgO) is added to the bulk Gibbs energy of the products $[\Delta_f G^o(MgO_{bulk}) + \Delta_f G^o(H_2O)]$ as in Figure 13.

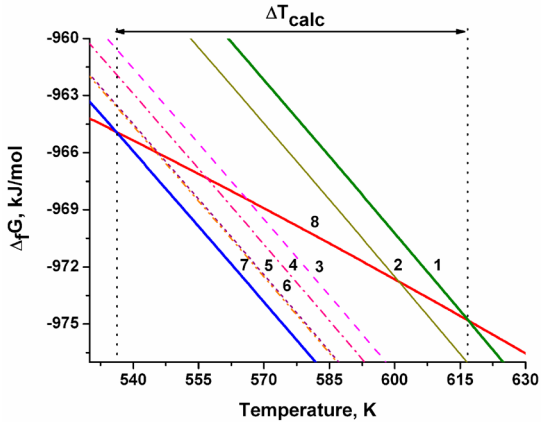

Figure 13. Estimated $\Delta G^o(T)$ values for the products SN/MO-Y: Y = 0 (1), 0.5 (2), 2 (3), 5 (4), 10 (5), 20 (6) wt %, bulk MgO (7) and $Mg(OH)_2$ (8).

Since S_{rea} = 13.8 $m^2/g \ll S_{pro}$ = 265 m^2/g we assumed the MH surface free energy $\Delta_{surf} G^o_{rea}$ to be zero and graphically determine the dehydration temperatures $T^*(Y)$ at various salt contents. The calculated difference $\Delta T_{calc}(Y) = T^*(Y) - T^*$(bulk) is displayed in Figure 14 together with the appropriate difference in the onset temperatures $\Delta T_{exp}(Y) = T_{onset}$[MH] − T_{onset} [SN/MH-Y] obtained from the DSC curves in Figure 2. The calculated depression exhibits similar behavior but is somewhat larger than the experimental results (except for Y = 0.5 wt %). Possible reasons maybe

(a) the initial $Mg(OH)_2$ has a nonzero surface energy, which may reduce $\Delta T_{calc}(Y)$;
(b) the MgO surface energy E_s is lower than 1.1 J/m^2 due to the presence of adsorbed water or the $NaNO_3$ interaction with MgO surface.

To the best of our knowledge, the surface energy of $Mg(OH)_2$ has not been precisely defined. However, it is certainly lower than that for MgO and lies between 0.05 and 0.5 J/m^2 as reported in ref 46. Hence, the surface energy $\Delta_{surf} G^o$(MH) can be estimated as $E_s \cdot S_{rea}$ = 0.7−7 J/g MH, which is, indeed, negligible as compared with 250 J/g MH for the product (MgO).

dx.doi.org/10.1021/am505418z | ACS Appl. Mater. Interfaces 2014, 6, 19966−19977

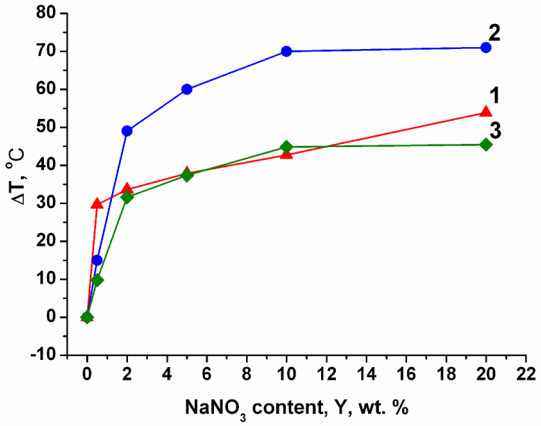

Figure 14. Experimental (1) and calculated (2 and 3) differences in the dehydration temperature as a function of the salt content. For curves 2 and 3 we assume E_s = 1.1 and 0.69 J/m^2, respectively.

Water adsorption may strongly reduce the E_s value for MgO. If it drops to 0.6 J/m^2, the surface energy $\Delta_{surf}G^o$(MgO) also decreases, and the calculated difference $\Delta T_{calc}(Y)$ aligns with the experimental one quite well (Figure 14).

The Nitrate–Hydroxide Interaction. The combination of DSC, XRD, Raman, FTIR, and XPS techniques provides insight into the interaction between the modifying salt and the host hydroxide. The interaction between $NaNO_3$ and $Mg(OH)_2$ starts during the SN/MH-Y sample preparation and enhances during their dehydration and rehydration. This interaction manifests itself as

(1) dramatic lowering of the apparent melting heat of $NaNO_3$ in SN/MH-Y;
(2) broadening of the $NaNO_3$ peaks at 220–270 °C (Figure 8), which may be due to a disordering of $NaNO_3$ lattice caused by the salt interaction with $Mg(OH)_2$. The peak widening may also be due to splitting this reflection into two peaks, which might be discerned at 240–270 °C (Figure 15). Variations of the intensity of (006) and the half-width of (104) reflexes of $NaNO_3$ at 220–270 °C correlate well with vanishing MH reflexes and appearing MgO reflexes (Figure 16);
(3) the Raman peak of $NaNO_3$ at 1068 cm^{-1} is split in the initial SN/MH-2 and SN/MH-10 giving a broad peak at 1051 cm^{-1} (Figure 11a). The latter may belong to a product of interaction between the salt and MH. After dehydration and subsequent rehydration this peak increases and becomes dominant at Y = 2% (Figure 11b). Similar splitting/broadening is found in the SN/MH-2 or SN/MH-10 FTIR spectra.

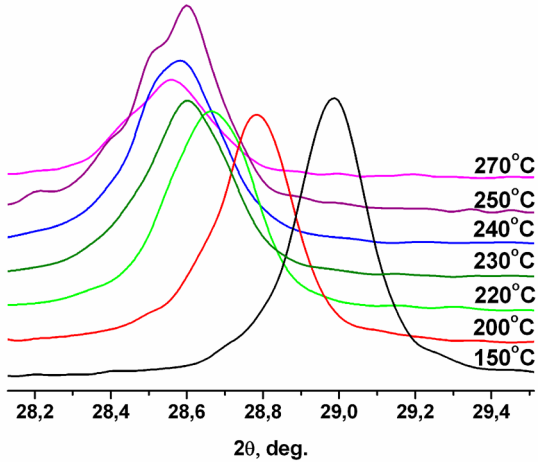

Figure 15. XRD patterns of (104) reflex of $NaNO_3$ for SN/MH-10.

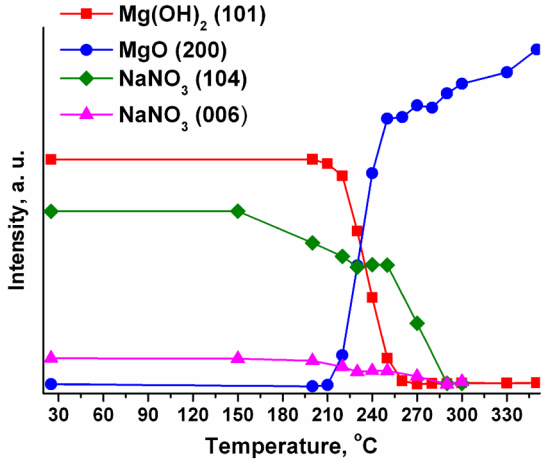

Figure 16. Intensities of $NaNO_3$ reflexes of SN/MH-10 at various temperatures.

All the data indicate that the state of nitrate in the SN/MH-Y mixtures is very different from that in the bulk. In particular, a part of the salt interacts with $Mg(OH)_2$ to form a highly defective or disordered phase that reveals itself as a peak/shoulder in XRD, Raman, and FTIR spectra.

This may be due to a substitution of hydroxyl groups by nitrate anions.

$$Mg{-}O{-}H + NO_3^- = Mg{-}O{-}NO_2 + OH^-$$

or

$$Mg{-}O{-}H\ H{-}O{-}Mg + NO_3^- = Mg{-}O{-}NO{-}O{-}Mg + 2OH^- + V^+$$

In the latter (bidentate) case, a positively charged defect V^+ of the $Mg(OH)_2$ lattice is formed to ensure charge conservation. Both types of interactions make the hydroxide more defective. Simultaneously, the inverse substitution

$$Na{-}NO_3 + OH^- = NO_3^- + NaOH$$

takes place in the salt lattice, which makes the salt nitrogen-depleted. Also, more hydroxyl groups move from the bulk closer to the sample surface. As XPS is a surface-sensitive method, vanishing of the N1s peak and slight enhancing of the O–H component of the O1s peak are observed. The symmetry of NO_3^- anion lowers. This symmetry lowering may result in the doublet formation at 1300–1500 cm^{-1} (IR) and 1000–1100 cm^{-1} (Raman).

The nucleation in $Mg(OH)_2$ is supposed to start on the surface,[22,33,47] and the reaction proceeds through a series of oxyhydroxide phases.[36,37,48] Therefore, the increase in the defect concentration in the vicinity of the surface may result in facilitation of oxyhydroxide nuclei formation. This would lead to shortening or even disappearance of the induction period.[49,50]

Formation of slit-shaped pseudomorph that is typical for MgO produced by dehydration of pure $Mg(OH)_2$ was not

dx.doi.org/10.1021/am505418z | ACS Appl. Mater. Interfaces 2014, 6, 19966–19977

registered for SN/MO-10. It is assumed here that at 350 °C an excessive amount of $NaNO_3$ interacts with the MgO surface and adheres/spreads on it. This could weaken intergrain contacts between the MgO crystallites and ultimately leads to collapsing macroscopic structure of the pseudomorph.

The typical size of the MgO crystallites in the pseudomorph, which is a product of the pure $Mg(OH)_2$ dehydration, is of 2−3 nm.[34] Such MgO has a high reactivity in many processes due to its high excessive surface energy. This state is essentially nonequilibrium, and its formation is governed by intralammelar and interlammelar strains that appear during the dehydration.[36] As the dehydration proceeds, these strains relax by disruption of the forming MgO crystals. This relaxation manifests itself as both fracturing and delamination.[36] For MgO, which is a product of SN/MH-Y dehydration, the nitrate ions may be bidentately linked to two adjacent brucite layers (Figure 17),

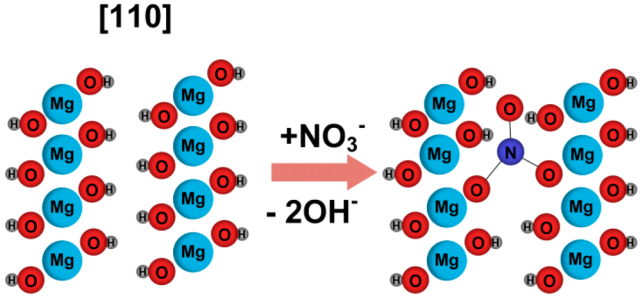

Figure 17. A schematic representation of bidentate embedment of NO_3^- ions in brucite layers.

which can create extra bonding between the brucite layers in addition to van der Waals forces and, therefore, leads to higher tensile strength of the forming oxide and coarser oxide particles.

New Impact for Storage of Middle-Temperature Heat. The observation of a lower decomposition temperature of reaction 1 in the presence of the salt is important because it allows for potential use of the waste heat with temperature levels lower than 300 °C, thus extending the list of heat sources available for TES.

Unfortunately, published data regarding waste heat availability is limited. This is especially true for the specific temperature grade of the waste heat obtainable from various industries. Useful estimations can still be made from reports of the International Energy Agency. For example, a huge quantity of heat (53.8×10^6 GJ) from hot stoves for steel production was wasted at temperature of ∼300 °C.[51,52] A temperature of 300 °C is not sufficient to decompose pure $Mg(OH)_2$; however, it is more than enough for dehydration of the new modified hydroxide. Similarly, waste heat from marine and locomotive diesel engines with exhaust temperature ≈ 325 °C[53,54] could also potentially be stored by the new materials with higher efficiency.

The dependence of the $Mg(OH)_2$ dehydration temperature on the $NaNO_3$ content provides an efficient way for harmonizing the energy accumulating reaction 4 with a particular heat source (Figure 1) in terms of the second law TES efficiency. Indeed, this efficiency considers not only the enthalpy balance but also the entropy generation during the TES process. The main source of the entropy production is a thermal coupling between an external heat source at temperature T_h and the heat storage unit at $T_r \leq T_h$. The entropy balance is given as $\Delta S = Q_{in}/T_r - Q_{in}/T_h = Q_{in}(T_h - T_r)/(T_h T_r) \geq 0$, where Q_{in} is the heat exchanged. Zero entropy generation corresponds to the case $T_h = T_r$, which means the energy-storing reaction proceeds right at $T = T_h$. This is possible only if equilibrium of reaction 4 is monovariant; that is, there is no decomposition at $T < T^*$; it starts and completes at $T_r = T^*$; the transition temperature is equal to the temperature of external heat source ($T_r = T_h$).

As discussed above, the equilibrium of reaction 4 is really monovariant, and a possible range of the T^* variation reaches 50 °C (Figure 2). That allows for fine adjustment of the reaction temperature to the temperature of a particular heat source to be stored.

The favorable kinetics of the modified $Mg(OH)_2$ decomposition facilitates its more widespread application and allows a high specific power of heat-storing process. The latter can be estimated from the half-conversion times presented in Figures 4 and 5. For instance, at 280 °C, $\tau_{0.5}$ = 21 min, which results in the average storage power of 1.1 kW/kg $Mg(OH)_2$. According to the literature,[55,56] this power level is very encouraging for heat transformation and makes possible the future design of very compact TES units.

CONCLUSIONS

The magnesium hydroxide dehydration exhibits thermodynamic characteristics that are excellent for long-term thermochemical storage of middle-temperature heat. However, the unfavorable kinetics of a pure $Mg(OH)_2$ dehydration at $T <$ 300 °C prevents its more widespread application. In the present article, we endeavor to solve this problem by modifying the magnesium hydroxide with sodium nitrate.

The focus of the research was on synthesis of $NaNO_3$-doped $Mg(OH)_2$, studying its thermal behavior and characterization of the dehydration products. It was found that even small $NaNO_3$ quantities (<2 wt %) considerably affect the dehydration temperature; for example, a 0.5% $NaNO_3$ additive reduces the temperature by ∼25 °C. The maximum decrease of decomposition temperature (∼50 °C) is observed with a salt content of 10−20 wt %. Thus, varying the $NaNO_3$ content is an efficient and convenient tool of managing the $Mg(OH)_2$ dehydration temperature within ∼50 °C range below that of pure $Mg(OH)_2$.

The dehydration kinetics of $Mg(OH)_2$ dehydration were studied by the TGA method at a fixed pressure of water vapor typical for TES systems with closed cycles as opposed to the majority of the literature studies, which were performed under vacuum. The sigmoid-to-exponential transformation of the dehydration dynamics observed in the presence of the salt indicates drastic changes in the dehydration pathways. DSC, HR-TEM, XRD, XPS, and BET analyses were applied to study the effects revealed and to elucidate possible ways of the $NaNO_3$ influence on the $Mg(OH)_2$ dehydration.

It was found that the morphology of the dehydration product (MgO) dramatically changes

(1) the formation of pseudomorph typical for the dehydration of pure $Mg(OH)_2$. This was not observed in the presence of $NaNO_3$ (HR-TEM);
(2) the MgO crystallites obtained in the doped system. These were several times larger than those that resulted from the pure hydroxide (XRD, BET).

Simultaneously, a disordering of the confined $NaNO_3$ was observed by XRD, Raman, and FTIR spectroscopy at the same temperature range when the decomposition started. This was

caused by the salt interaction with $Mg(OH)_2$ or/and MgO, for example, due to the substitution of hydroxyl groups by nitrate anions, which made the salt nitrogen-deficient (XPS). These changes in the local structure and composition of the salt and hydroxide can, in return, give rise to changing of the dehydration pathways. The increase in the defect concentration near the hydroxide surface could result in a shortening or even disappearance of the induction period (TGA). Embedding of nitrate ions between two adjacent brucite layers led to extra bonding between these layers, higher strength of the forming oxide, and coarser oxide particles (XRD, BET). The coarser MgO particles had lower specific surface area and smaller surface energy, which is profitable from a thermodynamic point of view and may also contribute to the observed depression of the dehydration temperature.

The modification of $Mg(OH)_2$ with sodium nitrate appeared to provide a valuable opportunity to control the decomposition rate, temperature, and the product texture. Reversibility of reaction 4 and rehydration processes will be addressed in a subsequent publication. The reported material $NaNO_3$/$Mg(OH)_2$ exhibited a large heat storage density and adjustable reaction temperature and may be a promising new candidate for TES at middle temperatures.

Although this conclusion is notable in itself, the authors believe that doping with inorganic salts may improve the kinetics and thermodynamics of decomposition of other hydroxides. Since there is a large number of possible combinations of salts and hydroxides, it may be expected that future academic research activities in this field will be vigorous. As a result, salt-doped hydroxides may well open a new generation of materials that might be applied in thermochemical storage of middle-temperature heat. For example, the authors have recently found that KNO_3 diminishes the dehydration temperature of $Ca(OH)_2$ by 30−40 °C. These decreases may be managed by varying the salt content in the range (0.5−5) wt %.[57] In a broader sense, the approach of modification by salts can be applied for improving the kinetics and thermodynamics of decomposition of other materials interesting for TES, such as carbonates. These possibilities will be further investigated in forthcoming studies.

■ ASSOCIATED CONTENT

Ⓢ Supporting Information

DSC curves for SN/MH-Y and their parameters, Arrhenius plot and half-conversion times, HR-TEM images of initial and dehydrated MH and SN/MH-10, XPS spectra. This material is available free of charge via the Internet at http://pubs.acs.org.

■ AUTHOR INFORMATION

Corresponding Author

*E-mail: aristov@catalysis.ru.

Notes

The authors declare no competing financial interest.

■ ACKNOWLEDGMENTS

The authors gratefully acknowledge contribution from Dr. S. Kosheev on measuring XPS spectra.

■ ABBREVIATIONS

TES, thermochemical energy storage
DSC, differential scanning calorimetry
TGA, thermogravimetric analysis
XRD, X-ray diffraction
CSR, coherent scattering region
HR-TEM, high-resolution transmission electron microscopy
XPS, X-ray photoelectron spectroscopy
MH, magnesium hydroxide
SN/MH-Y, sodium nitrate/magnesium hydroxide with *Y* weight % of sodium nitrate

■ REFERENCES

(1) Adams, T. A.; Nease, J.; Tucker, D.; Barton, P. I. Energy Conversion with Solid Oxide Fuel Cell Systems: A Review of Concepts and Outlooks for the Short- and Long-Term. *Ind. Eng. Chem. Res.* **2013**, *52*, 3089−3111.

(2) Polat, D. B.; Lu, J.; Abouimrane, A.; Keles, O.; Aminte, K. Nanocolumnar Structured Porous Cu-Sn Thin Film as Anode Material for Lithium-Ion Batteries. *ACS Appl. Mater. Interfaces* **2014**, *6*, 10877−10885.

(3) Ko, J. K.; Wiaderek, K. M.; Pereira, N.; Kinnibrugh, T.; Kim, J.; Chupas, P.; Chapman, K.; Amatucci, G. Transport, Phase Reactions, and Hysteresis of Iron Fluoride and Oxyfluoride Conversion Electrode Materials for Lithium Batteries. *ACS Appl. Mater. Interfaces* **2014**, *6*, 10858−10869.

(4) Hines, D. A.; Kamat, P. V. Recent Advances in Quantum Dot Surface Chemistry. *ACS Appl. Mater. Interfaces* **2014**, *6*, 3041−3057.

(5) Engel, J. H.; Alivisatos, A. P. Postsynthetic Doping Control of Nanocrystal Thin Films: Balancing Space Charge to Improve Photovoltaic Efficiency. *Chem. Mater.* **2014**, *26*, 153−162.

(6) Gutowska, A.; Li, L.; Shin, Y.; Wang, C. M.; Li, X. S.; Linehan, J. C.; Smith, R. S.; Kay, B. D.; Schmid, B.; Shaw, W.; Gutowski, M.; Autrey, T. Nanoscaffold Mediates Hydrogen Release and the Reactivity of Ammonia Borane. *Angew. Chem., Int. Ed.* **2005**, *44*, 3578−3582.

(7) Silambarasan, D.; Surya, V. J.; Vasu, V.; Iyakutti, K. Single Walled Carbon Nanotube−Metal Oxide Nanocomposites for Reversible and Reproducible Storage of Hydrogen. *ACS Appl. Mater. Interfaces* **2013**, *5* (21), 11419−11426.

(8) Kato, Y. Chemical Energy Conversion Technologies for Efficient Energy Use in *Thermal Energy Storage for Sustainable Energy Consumption;* Paksoy, H., Ed; Springer: New York, 2007; pp 377−391.

(9) Cabeza, L. F.; Castell, A.; Barreneche, C.; de Gracia, A.; Fernandez, A. I. Materials Used as PCM in Thermal Energy Storage in Buildings: A Review. *Renewable Sustainable Energy Rev.* **2011**, *15*, 1675−1695.

(10) Khutia, A.; Rammelberg, H.; Schmidt, T.; Henninger, S.; Janiak, C. Water Sorption Cycle Measurements on Functionalized MIL-101Cr for Heat Transformation Application. *Chem. Mater.* **2013**, *25*, 790−798.

(11) Dinçer, I.; Rosen, M. *Thermal Energy Storage: Systems and Applications,* 2nd ed.; John Wiley & Sons: Chichester, U.K., 2011.

(12) Ervin, G. J. Solar Heat Storage Using Chemical Reactions. *Solid State Chem.* **1977**, *22*, 51−61.

(13) Kato, Y.; Sasaki, Y.; Yoshizawa, Y. Magnesium oxide/water Chemical Heat Pump to Enhance Energy Utilization of a Cogeneration System. *Energy* **2005**, *30*, 2144−2155.

(14) Barin, I. *Themrochemical Data of Pure Substances;* VCH: Weinheim, Germany, 1989.

(15) Ryu, J.; Takahashi, R.; Hirao, N. Effect of Transition Metal Mixing on Reactivities of Magnesium Oxide for Chemical Heat Pump. *J. Chem. Eng. Jpn.* **2007**, *40*, 1281−1286.

(16) Kato, Y.; Takahashi, R.; Sekiguchi, T.; Ryu, J. Study on Medium-temperature Chemical Heat Storage Using Mixed Hydroxides. *Int. J. Refrig.* **2009**, *32*, 661−666.

(17) Ishitobi, H.; Uruma, K.; Takeuchi, M.; Ryu, J.; Kato, Y. Dehydration and Hydration Behavior of Metal-salt-modified Materials for Chemical Heat Pumps. *Appl. Therm. Eng.* **2013**, *50*, 1639−1644.

(18) Myagmarjav, O.; Ryu, J.; Kato, Y. Lithium bromide-mediated Reaction Performance Enhancement of a Chemical Heat-Storage

Material for Magnesium Oxide/Water Chemical Heat Pumps. *Appl. Therm. Eng.* **2014**, *63*, 170−176.
(19) Shkatulov, A.; Ryu, J.; Kato, Y.; Aristov, Yu. Composite Material "$Mg(OH)_2$/Vermiculite": A Promising New Candidate for Storage of Middle Temperature Heat. *Energy* **2012**, *44*, 1028−1034.
(20) Tang, X.; Guo, L.; Chen, C.; Liu, Q.; Li, T.; Zhu, Y. The Analysis of Magnesium Oxide Hydration in Three-phase Reaction System. *J. Solid State Chem.* **2014**, *213*, 32−37.
(21) Klug, H. P.; Alexander, L. E. *X-ray Diffraction Procedures for Polycrystalline and Amorphous Materials,* 2nd ed.; John Wiley & Sons: New York, 1974.
(22) Anderson, P. J.; Horlock, R. F. Thermal Decomposition of Magnesium Hydroxide. *Trans. Faraday Soc.* **1962**, *58*, 1993−2004.
(23) Gregg, S. J.; Razouk, R. I. The kinetics of the Thermal Decomposition of Magnesium Hydroxide. *J. Chem. Soc.* **1949**, *1*, S36−S44.
(24) Gordon, R. S.; Kingery, W. D. Thermal Decomposition of Brucite: II, Kinetics of Decomposition in Vacuum. *J. Am. Ceram. Soc.* **1967**, *50*, 8−14.
(25) Halikia, I.; Neou-Syngouna, P.; Kolitsa, D. Isothermal Kinetic Analysis of the Thermal Decomposition of Magnesium Hydroxide Using Thermogravimetric Data. *Thermochim. Acta* **1998**, *320*, 75−88.
(26) *Handbook of X-ray photoelectron spectroscopy;* Moulder, J. F., Stickle, W. F., Sobol, P. E., Eds.; Perkin-Elmer Corporation, Physical Electronics Division: Eden Prairie, MN, 1992.
(27) Rapoport, E. J. Polymorphism and Melting in the Alkali Nitrates to 40 kb with Some Comments on the Alkaline Earth Carbonates. *J. Phys. Chem. Solids* **1966**, *27*, 1349−1363.
(28) Lowings, M. G.; McCurdy, K. G.; Hepler, L. G. Heats of Melting of Sodium Nitrate and Indium by Differential Scanning Calorimetry: a Suggestion for a New Calibration Substance. *Thermochim. Acta* **1978**, *23*, 365−370.
(29) Angell, C. A.; Helphrey, D. B. Corresponding states and the glass transition for alkali metal nitrates. *J. Phys. Chem.* **1971**, *75*, 2306−2312.
(30) Criado, J. M.; Morales, J. On the Thermal Decomposition Mechanism for Dehydroxylation of Alkaline-Earth Hydroxides. *J. Therm. Anal.* **1976**, *10*, 103.
(31) Galwey, A. K.; Brown, M. E. *Thermal decomposition of ionic solids;* Elsevier: Amsterdam, The Netherlands, 1999; 271.
(32) Kazimirov, V. Yu.; Smirnov, M. B.; Bourgeois, L.; Guerlou-Demourgues, L.; Servant, L.; Balagurov, A. M.; Natkaniec, I.; Khasanova, N. R.; Antipov, E. V. Atomic Structure and Lattice Dynamics of Ni and Mg Hydroxides. *Solid State Ionics* **2010**, *181*, 1764−1770.
(33) Goodman, J. F. The Decomposition of Magnesuim Hydroxide in an Electron Microscope. *Proc. R. Soc. A* **1958**, *247*, 346.
(34) Moodie, A. F. Warble C. F. MgO Morphology and the Thermal Transformatuion of $Mg(OH)_2$. *J. Cryst. Growth* **1986**, *74*, 89−100.
(35) Matabola, K. P.; van der Merwe, E. M.; Strydom, C. A.; Labuschagne, F. The Influence of Hydrating Agents on the Hydration of Industrial Magnesium Oxide. *J. Chem. Technol. Biotechnol.* **2010**, *85*, 1569−1574.
(36) McKelvy, M. J.; Sharma, R.; Chizmeshya, A. V. G.; Carpenter, R. W.; Streib, K. Magnesium Hydroxide Dehydroxylation: In Situ Nanoscale Observations of Lamellar Nucleation and Growth. *Chem. Mater.* **2001**, *13*, 921−926.
(37) Sharma, R.; McKelvy, M. J.; Béarat, H.; Chizmeshya, A. V. G.; Carpenter, R. W. In-situ Nanoscale Observations of the $Mg(OH)_2$ Dehydroxylation and Rehydroxylation Mechanisms. *Philos. Mag.* **2004**, *84*, 2711−2729.
(38) Naono, H. Micropore Formation due to Thermal Decomposition of Magnesium Hydroxide. *Colloids Surf., A* **1989**, *37*, 55−70.
(39) Kim, M. G.; Dahmen, U.; Searcy, A. W. Structural Transformations in the Decomposition of $Mg(OH)_2$ and $MgCO_3$. *J. Am. Ceram. Soc.* **1987**, *70*, 146−154.
(40) Duffy, T. S.; Meade, C.; Fei, Y.; Mao, H.-K.; Hemley, R. J. High-pressure Phase Transition in Brucite, $Mg(OH)_2$. *Am. Mineral.* **1995**, *80*, 222−230.
(41) Nakagawa, I.; Walter, J. L. Optically Active Crystal Vibrations of the Alkali-Metal Nitrates. *J. Chem. Phys.* **1969**, *51*, 1389−1397.
(42) Brooker, M.; Irish, D. Crystalline-field Effects on the Infrared and Raman Spectra of Powdered Alkali-metal, Silver, and Thallous Nitrates. *Can. J. Chem.* **1970**, *48*, 1183.
(43) Jura, G.; Garland, C. W. The Experimental Determination of the Surface Tension of Magnesium Oxide. *J. Am. Chem. Soc.* **1952**, *74*, 6033−6034.
(44) Hayun, S.; Tran, T.; Ushakov, S. V.; Thron, A. M.; Van Benthem, K.; Navrotsky, A.; Castro, R. H. R. Experimental Methodologies for Assessing the Surface Energy of Highly Hygroscopic Materials: The Case of Nanocrystalline Magnesia. *J. Phys. Chem. C* **2011**, *115*, 23929−23935.
(45) Westwood, A. R.; Goldheim, D. L. Cleavage Surface Energy of {100} Magnesium Oxide. *J. Appl. Phys.* **1963**, *34* (11), 3335.
(46) Churakov, S. V.; Iannuzzi, M.; Parrinello, M. Ab Initio Study of Dehydroxylation−Carbonation Reaction on Brucite Surface. *J. Phys. Chem. B* **2004**, *108*, 11567.
(47) Yoshida, T.; Tanaka, T.; Yoshida, H.; Funabiki, T.; Yoshida, S.; Murata, T. Study of Dehydration of Magnesium Hydroxide. *J. Phys. Chem.* **1995**, *99*, 10890−10896.
(48) Freund, F.; Martens, R.; Scheikh-ol-Eslami, N. Recrystallization Effect During the Dehydration of Magnesium Hydroxide. *J. Therm. Anal.* **1975**, *8*, 525−529.
(49) Schmalzried, H. *Chemical kinetics of solids;* Wiley-VCH: Weinhem, Germany, 1995; 162.
(50) Galwey, A. K.; Brown, M. E. *Thermal decomposition of ionic solids*; Elsevier: Amsterdam, The Netherlands, 1999; 76.
(51) Mandil, C. *Tracking industrial energy efficiency and CO_2;* International Energy Agency: Paris, France; 2009.
(52) *Profiting from low-grade heat;* The Watt Committee on Energy Report No. 26; The institution of Electrical Engineers: London, U.K.; 1994.
(53) Hountalas, D. Prediction of Marine Diesel Engine Performance Under Fault Conditions. *Appl. Therm. Eng.* **2000**, *20*, 1753−1783.
(54) Shu, J. Z.; Wang, R. Z.; Lu, Y. Z.; Wu, J. Y. Operational Aspects of Adsorption Air-conditioner Used in Diesel Locomotive. *Int. J. Energy Res.* **2006**, *30*, 1377−1390.
(55) Aristov, Yu. I. Challenging Offers of Material Science for Adsorption Heat Transformation: A Review. *Appl. Therm. Eng.* **2013**, *50*, 1610−1618.
(56) Deng, J.; Wang, R. Z.; Han, G. Y. A Review of Thermally Activated Cooling Technologies for Combined Cooling, Heating and Power Systems. *Prog. Energy Combust. Sci.* **2011**, *37*, 172−203.
(57) Shkatulov, A. I.; Aristov, Y. I. Salt-modified Calcium Hydroxide: a New Candidate for Middle Temprature Heat Storage. In *Materials of IMPRES 2013 conference*; Research Publishing Services: Singapore, 2013; pp 643−649.